Photoacoustics 26 (2022) 100353

Contents lists available at ScienceDirect

Photoacoustics

journal homepage: www.elsevier.com/locate/pacs

Ultra-sensitive ppb-level methane detection based on NIR all-optical photoacoustic spectroscopy by using differential fiber-optic microphones with gold-chromium composite nanomembrane

Hanping Xiao [a,b,1], Jinbiao Zhao [a,b,1], Chaotan Sima [a,b,*], Ping Lu [a,b,*], Yanhong Long [a], Yan Ai [a], Wanjin Zhang [a], Yufeng Pan [a], Jiangshan Zhang [c], Deming Liu [a]

[a] Wuhan National Laboratory for Optoelectronics (WNLO) and National Engineering Laboratory for Next Generation Internet Access System, School of Optical and Electronic Information, Huazhong University of Science and Technology, Wuhan 430074, China
[b] Shenzhen Huazhong University of Science and Technology Research Institute, Shenzhen 518000, China
[c] Department of Electronics and Information Engineering, Huazhong University of Science and Technology, Wuhan 430074, China

ARTICLE INFO

Keywords:
Infrared
Photoacoustic spectroscopy
Fiber-optic microphone
Gas detection

ABSTRACT

In this paper, we propose and experimentally demonstrate an ultra-sensitive all-optical PAS gas sensor, incorporating with a near-infrared (NIR) diode laser, fiber-optic microphones (FOMs) and a double channel differential T-type photoacoustic cell. The FOM is realized by Fabry-Perot interferometry and novel gold-chromium (Au-Cr) composite nanomembranes. To meet the demand of high sensitivity and flat frequency response for the FOMs, the Au-Cr composite diaphragm is deliberately designed and fabricated by E-beam evaporation deposition with 330 nm in thickness and 6.35 mm in radius. Experimental results show that the FOM has a sensitivity of about 30 V/Pa and a flat frequency response from 300 to 900 Hz with fluctuation below 1 dB. Moreover, a double channel differential T-type photoacoustic cell is designed and employed in the all-optical PAS gas sensor, with the first-order resonant frequency of 610 Hz. The all-optical gas sensor is established and verified for CH_4 detection and the normalized noise equivalent absorption (NNEA) is 4.42×10^{-10} W•cm^{-1}•Hz$^{-1/2}$. The minimum detection limit (MDL) of 36.45 ppb is achieved with a 1 s integration time. The MDL could be further enhanced to 4.87 ppb with an integration time of 81 s, allowing ultra-sensitive trace gas detection.

1. Introduction

Methane (CH_4), a colorless, odorless, flammable and explosive gas, plays an important role in environmental atmospheric monitoring, clinical diagnosis and industrial control [1–3]. According to the 2021 WMO Greenhouse Gas Bulletin [4], the concentration of methane in the atmosphere is about 1.8 ppm and arises yearly, which contributes to the greenhouse effect. Therefore, it is of great significance to implement accurate and sensitive CH_4 detection. Beyond conventional methods such as electro-chemistry and gas chromatography [5,6], optical methods allow improved selectivity and sensitivity as well as fast response. Optical methods using laser absorption spectroscopy (LAS) based on the 'finger-print' absorption lines of molecules, such as tunable diode laser absorption spectroscopy (TDLAS), cavity ring-down spectroscopy (CRDS) and photoacoustic spectroscopy (PAS) [7–10], have been widely investigated for trace gas detection. TDLAS-based sensors have been widely commercialized [11], and it fundamentally relies on the long optical path and superior photodetectors to achieve favorable sensing performance. Also, ultra-stable cavity mode is essential in CRDS, which limits practical implementations.

PAS is acknowledged as an indirect method for trace gas sensing based on the photoacoustic effect. The photoacoustic effect refers to the principle that optical absorption of gas molecules results in localized heating and then generates gas vibration, which produces the acoustic pressure wave detected by an acoustic sensor i.e. microphone [12]. The PAS sensor has the special advantages of no wavelength selectivity and proportional to the laser power. Benefit from the development of laser technology, high power or mid-infrared laser is used in the PAS sensor to

* Corresponding authors at: Wuhan National Laboratory for Optoelectronics (WNLO) and National Engineering Laboratory for Next Generation Internet Access System, School of Optical and Electronic Information, Huazhong University of Science and Technology, Wuhan 430074, China
E-mail addresses: smct@hust.edu.cn (C. Sima), pluriver@mail.hust.edu.cn (P. Lu).
[1] H.X. and J.Z. made equal contribution with respect to this work.

https://doi.org/10.1016/j.pacs.2022.100353
Received 13 January 2022; Received in revised form 8 April 2022; Accepted 8 April 2022
Available online 12 April 2022

obtain high detection sensitive [13,14]. For example, Wu et al. reported a 3.3 μm inter-band cascade laser (ICL) in the quartz-enhanced photoacoustic spectroscopy (QEPAS) system to improve detection sensitivity [13]. Chen et al. reported a PAS sensor combined a high power near-infrared (NIR) laser with an erbium-doped fiber amplifier (EDFA), the output laser power up to 1 W [14]. Nevertheless, the use of ICL or EDFA made the sensor complex and costly, compared to single near-infrared diode laser.

Beside optical sources, photoacoustic cells and microphones are the other key components in the PAS gas sensor. Initially, electrical microphones were widely used in PAS due to low cost and excellent stability [15]. However, there are restrictions in electrical microphones such as electromagnetic interference and low sensitivity. Attributed to compact size, high sensitivity, remote sensing and immunity to electromagnetic interference, fiber-optic microphone (FOM) have been investigated in past decades [16–20]. To be noted, reported diaphragms such as polymer and graphene composite used in optical microphones still have several limitations in the application [19,20]. The relatively low reflectivity of most non-metallic material diaphragm results in additional attenuation and noise. On the other hand, the unstable chemical properties of the diaphragm material bring the risk of performance degradation as working in harsh environment, which may restrict the gas sensing performance and could be enhanced. Moreover, considering relatively high resonant frequency of traditional H-type photoacoustic cell [21], the optical microphones often have a small area to obtain a larger flat response range to match the photoacoustic cell, but this would lead to lower sensitivity of the diaphragm. Taking account into the different boundary conditions of the T-type photoacoustic cell, lower resonance frequency and fast response can be obtained simultaneously compared to the traditional H-type cell [22]. However, existed acoustic wave antinodes at the end facet of the reported single channel T-type cell may lead to excessive signal noise due to optical window absorption and environmental interference.

In this paper, we propose and demonstrate an ultra-sensitive all-optical PAS methane sensor incorporating with a pair of novel fiber-optic microphones (FOMs) and a double channel differential T-type photoacoustic cell. The acoustic signals are detected by two Fabry-Perot (FP) interferometric fiber-optic microphones with novel composite Au-Cr diaphragm and demodulated by the intensity-based quadrature point (Q-point) method. The proposed composite Au-Cr nanomembranes are designed by diaphragm forced vibration and fabricated by E-beam evaporation deposition with 330 nm in thickness (gold of 300 nm and chromium of 30 nm) and 6.35 mm in radius, achieving high acoustic sensitivity and flat frequency response. Moreover, a novel double channel differential T-type photoacoustic cell with the first-order resonant frequency of 610 Hz is designed and fabricated to match the proposed FOM for sensitivity enhancement. The wavelength modulation spectroscopy and second-harmonic detection (WMS-2*f*) with a low cost 1.65 μm DFB laser is employed to eliminate the fundamental frequency noise and increase signal noise ratio [23]. This all-optical PAS gas sensor is established and verified for CH_4 detection and the MDL of 36.45 ppb is achieved with a 1 s integration time. It could be further enhanced to 4.87 ppb with an integration time of 81 s, allowing ultra-sensitive trace gas sensing in versatile applications.

2. Experiment section

2.1. Design of the composite diaphragm and FOM

The essential acoustic detector directly determines the sensitivity and detection limit of the PAS sensor. For the diaphragm-based Fabry-Perot interferometric FOM, the vibration of diaphragm converts the acoustic signal into the variation of reflection spectrum. According to the membrane model for diaphragm vibration analysis, the tension of the diaphragm makes the diaphragm deformation to recover [24]. Based on the forced vibration of the diaphragm structure, the main influence on the sensitivity performance of the FOM is the deformation at the center of the circular diaphragm. By normalizing the deformation at the center of the diaphragm (r = 0), the vibration sensitivity S_m (nm/Pa) and the first-order resonant frequency f_1 (Hz) can be calculated through the forced vibration equation by Eq. (1) and Eq. (2):

$$S_m = \frac{1}{k_w^2 Ph}\left[\frac{1}{J_0(k_w a)} - 1\right] \tag{1}$$

$$f_1 = \frac{2.405}{2\pi a}\sqrt{\frac{P}{\rho}} \tag{2}$$

Where P, h, a, w, ρ, r is tensile stress, thickness, radius, angular frequency of acoustic, material density, radius in polar coordinates, respectively. k_w is set as $w/c = w/\sqrt{P/\rho}$. J_0 is zero-order Bessel function [25].

It is implied from Eq. (1) that the vibration sensitivity S_m could be directly improved by reducing diaphragm tension and thickness, as well as increasing material density and diaphragm radius. To be noted it could come across practical fabrication challenges, such as in the nanomembrane transferring process if the diaphragm is too thin. Gold diaphragm is primarily selected with high-density and chemical stability beyond other available materials. But in the metal nanomembranes deposition and transferring process, it is challenging to obtain thin layer and large proportion of pure gold nanomembrane simultaneously, due to tension and thermal effect. Here, a chromium substrate layer is introduced and a new type of Au-Cr composite diaphragm is proposed in our FOM. It is found that nanomembrane transferring process has been significantly upgraded by adding chromium as the substrate layer.

The composite diaphragm can be considered theoretically as a uniform elastic diaphragm and deforms gradually in the process of diaphragm transfer. This approximation allows the interface force between the composite diaphragms around the free edge and the substrate approaching a shear force. Excessive shearing force will cause nanomembranes wrinkles and even ruptures. When the external pulling force $t(x)$ works on the free end of diaphragm, it will produce a corresponding tension σ_m. It is acknowledged that tension at the edge of the diaphragm σ_m will evenly transfer to the entire interface. The governing equation $q(x)$ can be calculated by Eq. (3):

$$q(x) = \sigma_m\sqrt{\frac{kh_f}{2\pi x}} \tag{3}$$

where $q(x)$, h_f, σ_m, x is interface shear force with distance from diaphragm edge, thickness, free end of diaphragm tension and distance from diaphragm edge, respectively [26]. Where k can be described by Eq. (4):

$$k = \frac{E_s}{1-v_s^2}\cdot\frac{1-v_f^2}{E_f} \tag{4}$$

where $E_{s,f}$, $v_{s,f}$ is Young's modulus and Poisson's ratio of substrate and film. Chromium has a higher Young's modulus and a lower Poisson's ratio than gold, therefore Cr-Si interface have less shear force according to Eq. (3). The composite diaphragm has higher chance of diaphragm formation, whose interface shear force distribution is shown in Fig. 1.

Radius and thickness of the diaphragm play an important role in the FOM performance including frequency response and sensitivity characteristics. In terms of gold-chromium diaphragm, the bulk density and tensile stress of the diaphragm are set to 19,300 kg/m^3 and 50 MPa. Diaphragm response curve are obtained by changing radius and thickness of the diaphragm. As shown in Fig. 2, it is indicated that the diaphragm thickness merely affects the sensitivity with inverse proportion relationship, and the enlarged radius contributes to increase sensitivity but also brings lower resonant frequency.

Flat frequency response and optimized sensitivity are both required around the photoacoustic cell resonant frequency. With comprehensive analysis of sensitivity and response flatness characteristics, the

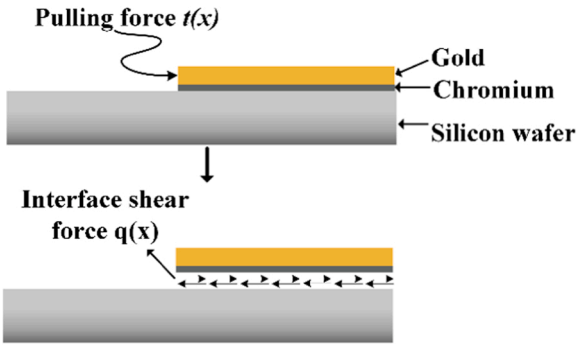

Fig. 1. The interface shear force distribution in the Au-Cr composite diaphragm.

composite Au-Cr diaphragm is designed optimized and fabricated by E-beam evaporation deposition. The composite nanomembranes of 330 nm thickness is realized with gold of 300 nm and chromium of 30 nm and 6.35 mm in radius. The detailed fabrication procedure for the metal nanomembranes and FOM package were discussed in our previous work [27]. The resonance frequency is calculated to be 3.1 kHz according to Eq. (2).

The schematic structure and packaged samples of the proposed FOM is shown in Fig. 3. A low-finesse Fabry-Perot interferometer is established with the fiber facet and the Au-Cr diaphragm. When an acoustic pressure is applied to the diaphragm, the FP cavity length will change. Therefore, reflected intensity can be approximately described by Eq. (5):

$$I_r = 2I_0[1 + B\cos(\varphi_0 + \varphi(t))] \quad (5)$$

Where I_0, B, φ_0, $\varphi(t)$ is the intensity of the incident light, the contrast of FOM, initial phase and phase to be measured [28]. The interference spectrum of the designed FOM (finesse number is about 2) was measured by the optical spectrum analyzer (AQ6370C-20, YOKOGAWA) as shown in Fig. 4. By choosing a proper wavelength, the FOM be operated in quadrature point (Q point, $\varphi_0 = (m+1/2)\pi$, m is an integer), which can make the FOM achieve maximum measurement sensitivity and dynamic range.

To characterize the performance of the designed FOM, measured frequency response with the frequency range of 100–2500 Hz is shown in Fig. 5. The sensor exhibits a flat frequency range between 300 and 900 Hz. The sensitivity fluctuation is less than 1 dB while the average sensitivity is about 30 V/Pa. In addition, the first-order resonant frequency is about 1.9 kHz, which separates from frequency domain for acoustic detection, and experimental results show that the two proposed FOMs have similar sensitivity. Compared with the reported pure metal

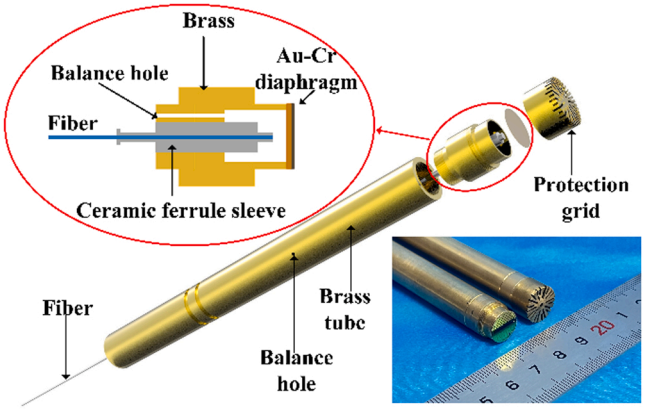

Fig. 3. Schematic of the structure of the proposed FOM.

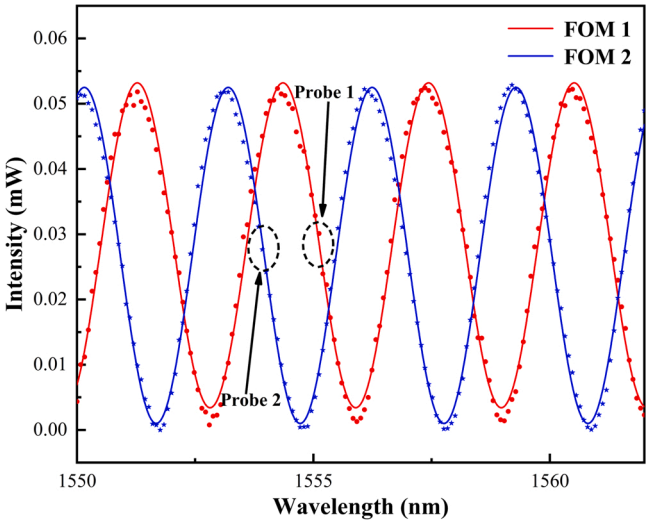

Fig. 4. Measured interference spectrums of the two FOMs with the probes showing the Q point demodulation.

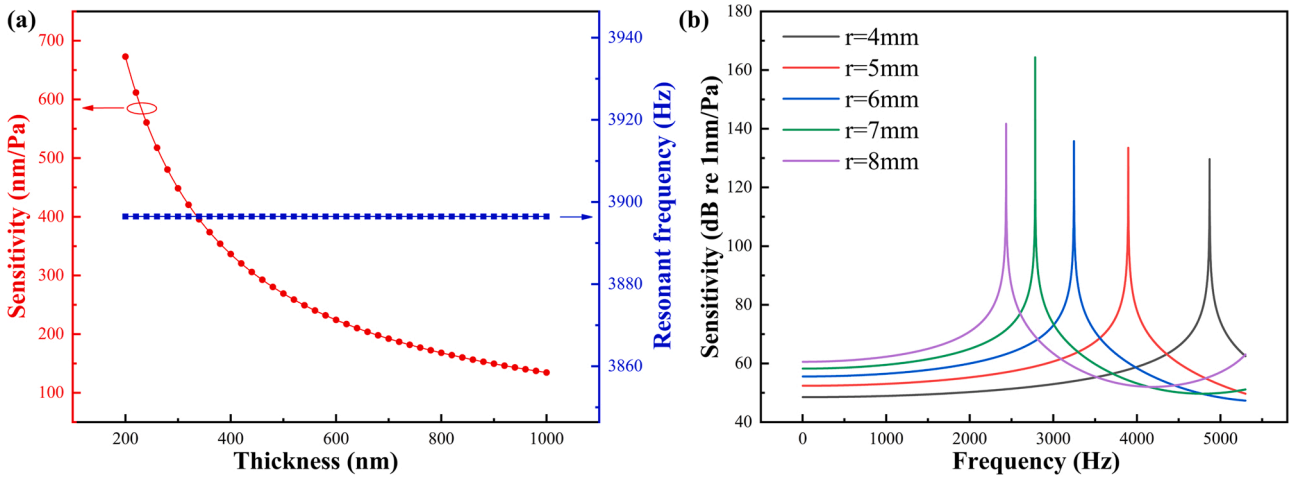

Fig. 2. Theoretical estimation of the influence of diaphragm parameters on sensitivity. (a) Influence of diaphragm thickness on sensitivity and resonant frequency, with operating frequency of 1 kHz and the nanomembrane radius of 6 mm. (b) Influence of diaphragm radius on sensitivity curve with the nanomembrane thickness of 300 nm.

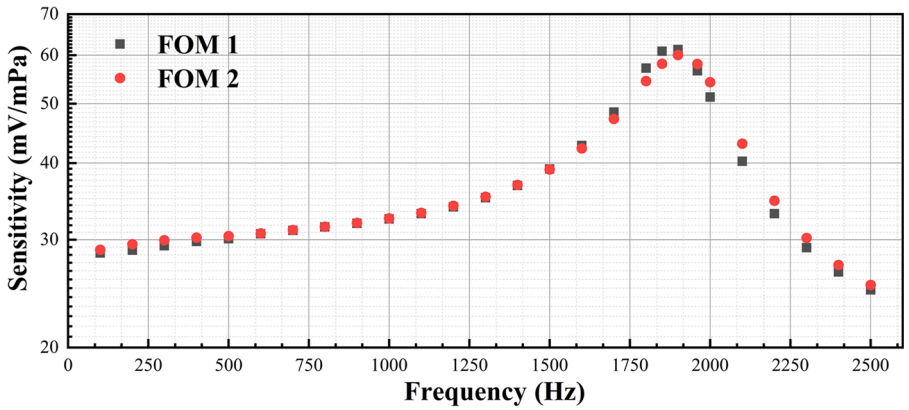

Fig. 5. The measured frequency responses of the two FOMs with the frequency range of 100–2500 Hz.

diaphragm, the composite diaphragm has a thinner thickness and larger radius to obtain ultra-high sensitivity and improved stability. In addition, benefits from the extremely stable physical and chemical properties of Cr and Au, the designed FOM can be applied in the measurement of corrosive or viscous gases for a certain long time.

2.2. Double channel differential T-type photoacoustic cell

A novel double channel differential T-type photoacoustic cell is designed and experimentally implemented in the PAS methane sensor. To optimize the performance of the system, a photoacoustic cell should be designed to match the FOM geometry and frequency. Compared with the conventional H-type cell, the T-type cell has a lower resonant frequency, a higher cell constant and faster response. For the T-type resonant PA cell, the 1st resonant frequency f can be calculated by Eq. (6):

$$f = \frac{v}{4(L + 8R/3\pi)} \tag{6}$$

Where v is the speed of sound in the sample gas, L and R are the radius and length of the resonator [29]. Moreover, longer length and smaller radius of the photoacoustic cell could be properly considered to increase the cell constant and photoacoustic signals.

The schematic design and 3D structure of the double channel differential T-type photoacoustic cell are shown in Fig. 6(a) and (b), respectively. The differential photoacoustic cell consists of two identical cylindrical channels as two photoacoustic resonators and one buffer volume at the near end of these channels. The inner radius and length of the identical channels are 4 mm and 120 mm. The inner radius and length of the buffer are 15 mm and 30 mm. A finite element model is constructed to simulate the acoustic field distributions at the first resonant frequency in the photoacoustic cell, as shown in Fig. 7(a). For the T-type differential cell, the end facet of the photoacoustic resonators exhibits the acoustic antinode, thus a pair of identical FOMs is located at the end of each channel to detect the maximum acoustic pressure. In addition, the acoustic wave phase is reversed for the photoacoustic resonators, resulting the acoustic signals are doubled [30]. Since only one channel is excited by the laser source, the background noise caused by window absorption and external environment are effectively suppressed by using a differential amplifier to subtract the signals from the pair of FOMs. The simulated frequency responses of the designed photoacoustic cell are shown in Fig. 7(b). The first-order resonant frequency of the designed photoacoustic cell is about 629 Hz, which is located in the flat response region of the FOM.

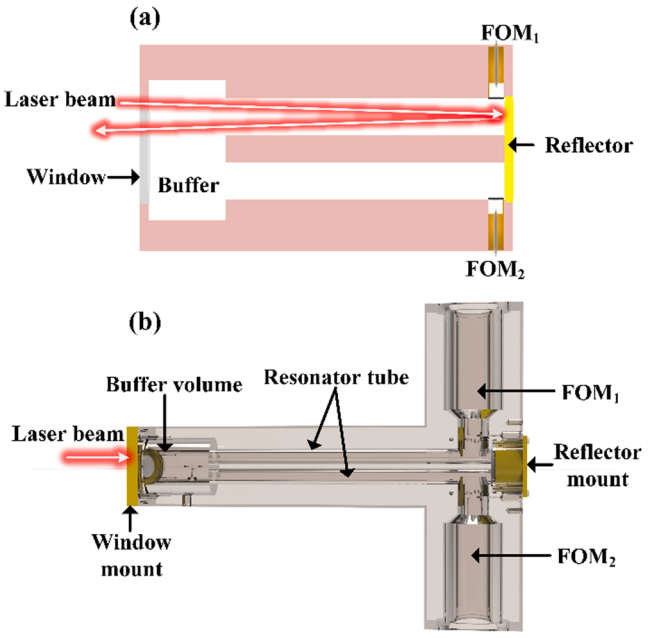

Fig. 6. (a) Schematic design and (b) 3D structure of the double channel differential T-type photoacoustic cell.

3. All-optical PAS gas sensor experiments

3.1. Experimental configuration

The WMS-2f experiment of the PAS methane sensor system is depicted in Fig. 8. A DFB laser (NTT NLK1U5EAAA) with a central wavelength of 1.65 μm is used as the excitation source to generate the photoacoustic signals. A laser driver (Wavelength Electronics, model LDTC0520) is used to control temperature and provide injection current, and the laser temperature and current are set at 29.5 ℃ and 97.5 mA respectively to align with the selected methane absorption line at 1650.96 nm. The measured laser output power of the DFB laser is 14.7 mW. According to the HITRAN2012 database [31], the absorption coefficient of CH_4 gas molecule at 1650.96 nm is 0.37 cm^{-1}, corresponding to line strength of 1.52×10^{-21} $cm^{-1}/(mol \bullet cm^{-2})$. An arbitrary waveform generator (Tektronix, Model AFG31102) is used to generate a sawtooth pattern with modulated sinusoidal wave. The sawtooth pattern is to sweep the laser central wavelength around the absorption line while the sinusoidal wave is used to modulate the laser wavelength for harmonics detection. The interaction of the modulated laser with the absorption line leads to the generation of signals at

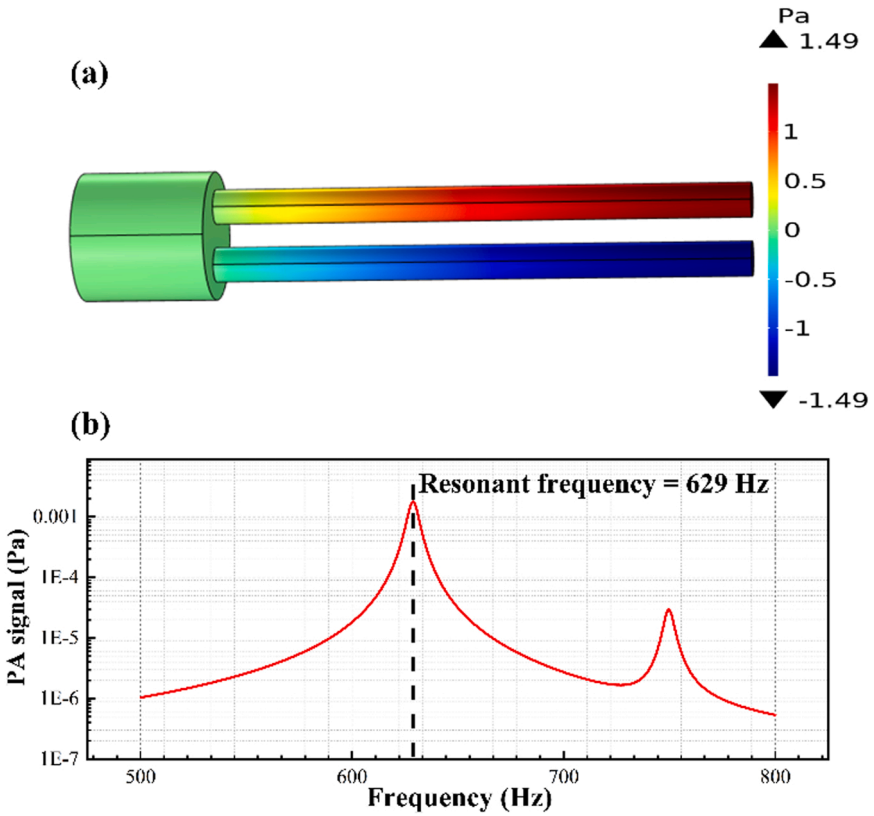

Fig. 7. (a) Simulated acoustic field distribution of the double channel differential T-type photoacoustic cell at the 1st resonant frequency (b) Simulated frequency responses of the double channel differential T-type photoacoustic cell.

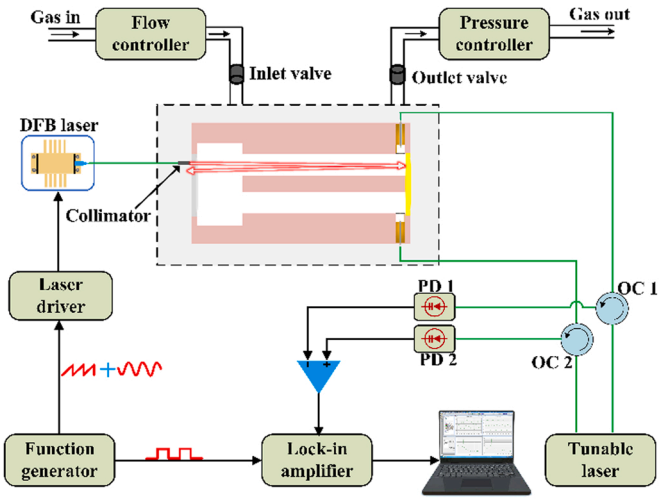

Fig. 8. Schematic experimental diagraph of the PAS sensor for CH_4 detection by using two fiber-optic microphones. PD: photoelectric detector; OC: optical circulator.

different harmonics of the modulation frequency, and the 2nd harmonic is used in the experiments.

The output laser beam is horizontal collimated into one photoacoustic channel of the T-type differential photoacoustic cell through a fiber collimator (OZ optical, Model LPC-01). A CaF_2 window with diameter of 20 mm and transmissivity efficiency of $> 95\%$ is mounted on the one side of the photoacoustic cell and a silver-plated reflector is mounted on the other side to double the absorption path length. Two identical FOMs are located to detect acoustic signals from two channels.

In the FOM signal demodulation part, a dual-channel narrow linewidth tunable laser (Alnair Labs, Model TLG-200) is used to connect to the fiber-optic microphones through optical circulators. The output wavelength of each channel is tuned to the Q-point of the interference spectrum of the two FOMs respectively. The interference spectrum is received by the photoelectric detector (New Focus, Model 1623) via the same optical circulator. The electrical signals are first processed by the differential pre-amplifier and then fed to a lock-in amplifier (LIA, Zurich Instruments, MFLI 500KHz) to demodulate the signals in a 2 *f* mode. The time constant and filter slope of the LIA are set to 1 s and 12 dB/Oct, corresponding to a detection bandwidth of 0.25 Hz. The demodulated signals are recorded and processed by the computer. The differential T-type photoacoustic cell has gas inlet and outlet controlled by two electromagnetic valves. The gas inlet was located near the ends of buffer volume. To ensure the gas exchange and diffusion within the photoacoustic cell, two gas outlets were symmetrically positioned at the end facet of two identical cylindrical channels. The PTFE membrane of 3 μm thickness and desiccant are set in the inlet to filter particles and water when monitoring the CH_4 in air. Two bottles of CH_4/N_2 standard gas (2% uncertainty) with 20 ppm and 500 ppm are diluted with pure N_2 gas to produce different concentrations by using a gas blender (MCQ Instruments, GB100, 1% uncertainty). A pressure controller and a flow meter are used to control the gas pressure and the flow rate within the gas pipeline.

3.2. *Optimization of the laser modulation frequency*

In the resonant PAS system, the acoustic signal maximizes when the laser modulation frequency agrees with the resonant frequency of the photoacoustic cell. The 1st resonant frequency of the designed photoacoustic cell is measured experimentally. The 50 ppm CH_4 is flowed photoacoustic the photoacoustic cell and the wavelength of the DFB laser is locked at 1650.96 nm for the CH_4 absorption line. The sinusoidal

modulation frequency of the laser is scanned from 230 Hz to 1050 Hz, and the WMS-2*f* signal is recorded to measure the frequency response from 460 Hz to 2100 Hz. As shown in Fig. 9, there is a peak value at the modulation frequency of 305 Hz, therefore the 1st resonant frequency of the optimized T-type photoacoustic cell is about 610 Hz, close to the simulation value of 629 Hz and located in the flat response region of the employed FOM. Compared with the Fig. 5, it is known that a peak value of 950 Hz is generated at the first-order resonant frequency of the proposed FOMs.

3.3. Optimization of the laser modulation amplitude

In order to improve the intensity of the 2nd acoustic harmonic, the laser modulation amplitude is optimized in this experiment. The DFB laser is thermostatically controlled, and the bias current is adjusted to set the laser wavelength to 1650.96 nm. The 310 Hz sinusoidal modulation current ranging from 1.5 mA to 17.5 mA is then superimposed to the bias current. The photoacoustic cell is filled with 50 ppm CH_4, and the output acoustic signal is recorded, as shown in Fig. 10. It is indicated that the optimal laser modulated bandwidth is about 11.78 GHz. Considering the full width at half maximum (FWHM) of the absorption line at 1650.96 nm being 4.64 GHz from the HITRAN database, the optimal laser modulation index is calculated to be 2.54 in the PAS sensor.

4. Results and discussion

In order to evaluate the performance of the PAS sensor for CH_4 detection, the parameters of this system are adjusted and setup properly. The CH_4 gases with different concentrations are obtained by the commercial gas blender. Various CH_4/N_2 mixture from 2 ppm to 500 ppm are flowed into the photoacoustic cell. The laser bias current is increased from 86 mA to 110 mA.

The relationship between single channel and differential double channels was investigated as shown in Fig. 11. It is shown that the magnitude of WMS-2*f* signals from the differential double channels basically doubled compared to that of the single channel. Furthermore, the inset shows that the phases of the acoustic waves from the two resonators are reversed, which are detected by two photoelectric detectors of the FOMs.

The WMS-2*f* signals of CH_4 with various concentrations are shown in Fig. 12(a). The sensor response curve is obtained by imposing a linear fit to the experimental data-points, characterized by an R^2 value of > 0.999 and a slope of 57.26 μV/ppm.

The background noise of the sensor is obtained by flushing pure N_2 into the photoacoustic cell with an integration time of 1 s, which is shown in Fig. 12(b). The background noise (1σ) is calculated to about 2 μV. The MDL could be estimated to be 36.45 ppb with the responsiveness of 57.26 μV/ppm, comparable with CH_4 sensors using mid-infrared lasers. The normalized noise equivalent absorption (NNEA), which is independent excitation source power and absorption strength, is calculated to be 4.42×10^{-10} W•cm^{-1}•Hz$^{-1/2}$ with the condition of 0.25 Hz detection bandwidth and 14.7 mW optical power.

For comparison, the performances of some state-of-the-art laser spectroscopy based CH_4 sensors are summarized in Table 1. To the best of our knowledge, the sensing NNEA and achieved MDL in this work are optimum among previously reported optical PAS methane sensors so far, even superior than those using mid-infrared laser sources. This gas sensor could be directly upgraded if using amplified near infrared laser or the mid-infrared laser source.

An Allan-Werle deviation analysis was conducted in pure N_2 to evaluate the long-term stability of the PAS CH_4 sensor [32,33], and the results are shown in Fig. 12(c). It is observed that the Allan deviation is

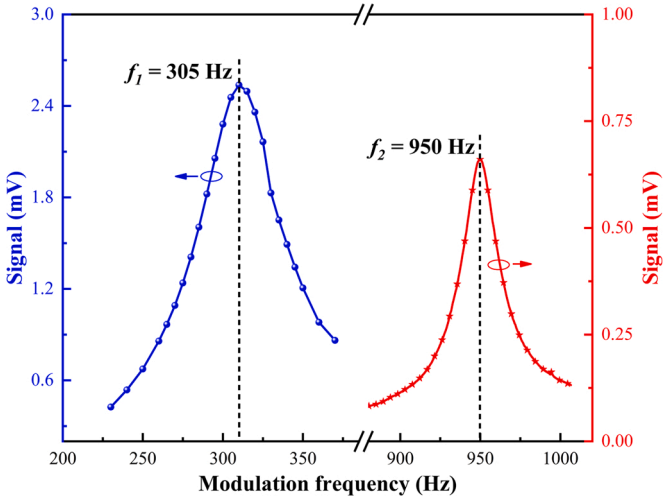

Fig. 9. The measured frequency responses of the all-optical PAS gas sensor.

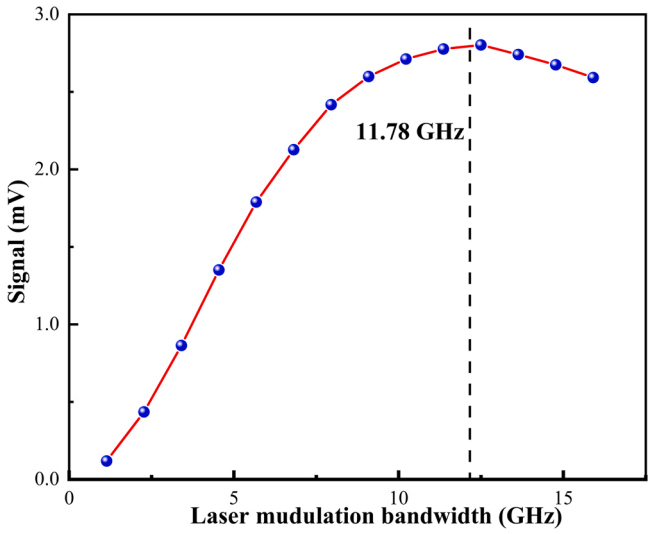

Fig. 10. Amplitude of WMS-2*f* signals as a function of laser modulated bandwidth.

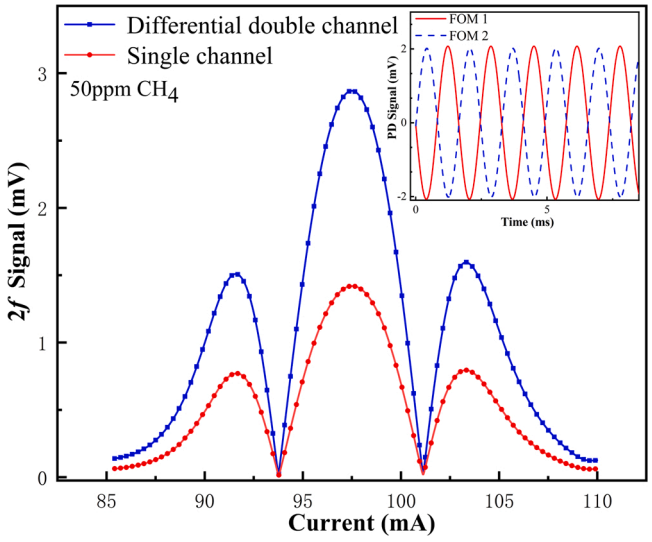

Fig. 11. The output WMS-2*f* signals from the single channel and from the differential double channel. In the inset are detected signals of the photoelectric detectors.

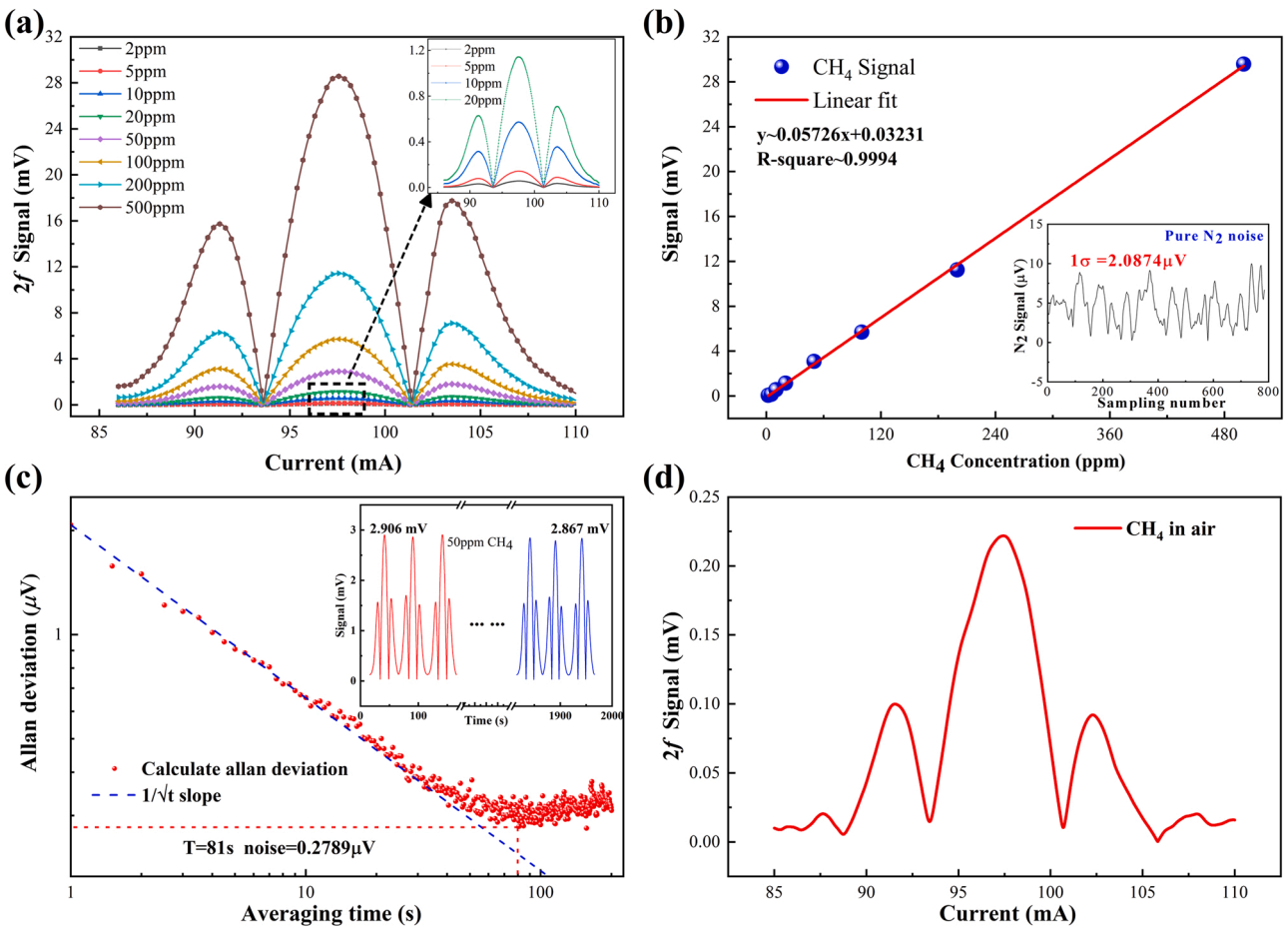

Fig. 12. (a) The output WMS-2*f* signals of CH_4 as function of concentration. (b) The output WMS-2*f* (maximum peak value) signals of CH_4 gas as function of gas concentration. Inset: the background noise of the optimized T-type resonant photoacoustic cell by filling the photoacoustic cell with pure N_2. (c) Allan variance analysis of the photoacoustic sensor. In the inset are output WMS-2*f* signals over 2000 s (d) The tested WMS-2*f* signals of CH_4 in the lab atmosphere.

Table 1
Performance indicators of methane sensors based on absorption spectroscopy.

Technology	Laser wavelength (nm)	Wavelength region	Power (mW)	MDL[a] (ppb)	NNEA ($W•cm^{-1}•Hz^{-1/2}$)	Ref
QEPAS	3300	Mid infrared	6.5	50	$2.9*10^{-9}$	[13]
PAS	3200	Mid infrared	2.8	3600	not stated	[34]
MPC[b] -TDLAS	1650.96	Near infrared	6.3	117	not stated	[35]
QEPAS	2300	Near infrared	6.3	2200	$2.0*10^{-9}$	[36]
All-optical PAS	1651	Near infrared	20	9@500 s	not stated	[22]
All-optical PAS	1650.9	Near infrared	12	8400	$2.1*10^{-8}$	[37]
All-optical PAS	**1650.96**	**Near infrared**	**14.7**	**36.45**	$\mathbf{4.42*10^{-10}}$	**[This paper]**

[a] The MDL is obtained with a 1 s integration time.
[b] MPC: Multi-pass cell.

0.2789 μ*V* for an integration time of 81 s. The corresponding MDL can be further improved to 4.87 ppb, extended Allan variance data can be obtained if further adding the PID feedback control to stabilize the Q point in the FOM demodulation [38].

Furthermore, the air in the laboratory environment is directly tested by the PAS sensor and the WMS-2*f* harmonic of CH_4 in air is shown in Fig. 12(d). It shows that the peak value of the 2 *f* harmonic is 0.225 mV, therefore the methane in the laboratory environment is measured to be around 3.365 ppm. With benefits of the optical fiber scheme, such as low transmission loss, intrinsic safety and immunity to electromagnetic interference, the demonstrated all optical PAS sensor shows potentials in the long-distance sensing for accurate trace gas detection.

5. Conclusions

In summary, a novel all-optical ultra-sensitive PAS CH_4 sensor is developed using a near infrared DFB laser. The essential composting diaphragmed FOMs and a differential T-type photoacoustic cell are designed and fabricated. Acoustic sensitivity and nanomembrane transfer success rate have be greatly improved by use of the novel Au-Cr composite diaphragm. The Au-Cr composite diaphragm is fabricated by E-beam evaporation deposition with 330 nm in thickness and 6.35 mm in radius. Compared with traditional electrical microphone, the FOM exhibits a high sensitivity of about 30 V/Pa and flat frequency response. Environmental and gas flow noise is inhibited and the acoustic signal is basically doubled by use of the unique multichannel differential T-type photoacoustic cell with the first-order resonant frequency of 610 Hz.

The MDL and NNEA of the PAS sensor are detected to be 36.45 ppb with a 1 s integration time and 4.42×10^{-10} W•cm^{-1}•Hz$^{-1/2}$. The MDL can be further decreased to 4.87 ppb with an integration time of 81 s. Atmospheric CH_4 in the lab has also been monitored verified by the PAS sensor. The experimental results indicate that ultra-sensitive CH_4 gas monitoring can be achieved by the use of a low cost near infrared DFB laser. The developed all optical PAS sensor in this paper shows the features of ultra-sensitivity and optical fiber connection with the all-optical configuration, which pave the way for remote and long-distance trace gas detection.

Declaration of Competing Interest

The authors declare that there are no conflicts of interest.

Acknowledgement

This work was supported by NSFC (No. 61775070), NSFC-RS Exchange Programme (No. 62111530153), Science Fund for Creative Research Groups of the Nature Science Foundation of Hubei (No. 2021CFA033), the Royal Society International Exchanges 2020 Cost Share (NSFC) of United Kingdom (No. IEC\NSFC\201015), Fund from Science, Technology and Innovation Commission of Shenzhen Municipality (2021Szvup089), and the Open Projects Foundation (No. SKLD2104) of State Key Laboratory of Optical Fiber and Cable Manufacture Technology (YOFC).

References

[1] K. Jawaharraj, N. Shrestha, G. Chilkoor, S.S. Dhiman, J. Islam, V. Gadhamshetty, Valorization of methane from environmental engineering applications: a critical review, Water Res. (2020), 116400, https://doi.org/10.1016/j.watres.2020.116400.

[2] H.F. Hammer, M.R. Fox, J. Keller, S. Salvatore, G. Basilisco, J. Hammer, L. Lopetuso, M. Benninga, O. Borrelli, D. Dumitrascu, B. Hauser, L. Herszenyi, R. Nakov, D. Pohl, N. Thapar, M. Sonyi, European guideline on indications, performance, and clinical impact of hydrogen and methane breath tests in adult and pediatric patients: European Association for Gastroenterology, Endoscopy and Nutrition, European Society of Neurogastroenterology and Motility, and European Society for Paediatric Gastroenterology Hepatology and Nutrition consensus, United Eur Gastroent (2021). ⟨https://doi.org/10.1002/ueg2.12133⟩.

[3] L. Zhang, H. Wang, C. Chen, P. Wang, L. Xu, Experimental study to assess the explosion hazard of CH4/coal dust mixtures induced by high-temperature source surface, Process Saf. Environ. (2021) 60–71. ⟨DOI: https://doi.org/10.1016/j.psep.2021.08.005⟩.

[4] WMO Greenhouse Gas Bulletin (GHG Bulletin) - No.17: The State of Greenhouse Gases in the Atmosphere Based on Global Observations Through 2020. ⟨https://library.wmo.int/index.php?lvl=notice_display&id=21975⟩.

[5] Y. Yang, Y. Tang, H. Jiang, Y. Chen, P. Wan, M. Fan, R. Zhang, S. Ullah, L. Pan, J. Zou, M. Lao, W. Sun, C. Yang, G. Zheng, Q. Peng, T. Wang, Y. Luo, X. Sun, A. S. Konev, O.V. Levin, P. Lianos, H. Zhuofeng, Z. Shen, Q. Zhao, Y. Wang, N. Todorova, C. Trapalis, M.V. Sheridan, H. Wang, L. Zhang, S. Sun, W. Wang, J. Ma, Roadmap on gas-involved photo- and electro- catalysis, Chin. Chem. Lett. 12 (2019) (2020) 2089–2109, https://doi.org/10.1016/j.cclet.2019.10.041.

[6] R. Wagner, D. Schönauer-Kamin, W. Bäther, R. Moos, Concept study with experimental proof for a new type of detector for gas chromatography, Sens. Actuators B Chem. (2021), 130490, https://doi.org/10.1016/j.snb.2021.130490.

[7] Q. Wang, Z. Wang, T. Kamimoto, Y. Deguchi, D. Wen, D. Takahara, Applications of TDLAS based multi-species hydrocarbon measurement using a wide scanning range DFG laser, Results Eng. (2021), 100297, https://doi.org/10.1016/j.rineng.2021.100297.

[8] A. Maity, S. Maithani, M. Pradhan, Cavity ring-down spectroscopy: recent technological advancements, techniques, and applications, Anal. Chem. 1 (2021) 388–416, https://doi.org/10.1021/acs.analchem.0c04329.

[9] F. Sgobba, A. Sampaolo, P. Patimisco, M. Giglio, G. Menduni, A.C. Ranieri, C. Hoelzl, H. Rossmadl, C. Brehm, V. Mackowiak, D. Assante, E. Ranieri, V. Spagnolo, Compact and portable quartz-enhanced photoacoustic spectroscopy sensor for carbon monoxide environmental monitoring in urban areas, Photoacoustics (2022), 100318, https://doi.org/10.1016/j.pacs.2021.100318.

[10] Y. Pan, L. Dong, X. Yin, H. Wu, Compact and highly sensitive NO2 photoacoustic sensor for environmental monitoring, Molecules 5 (2020) 1201, https://doi.org/10.3390/molecules25051201.

[11] B. Deng, C. Sima, Y. Xiao, X. Wang, Y. Ai, T. Li, P. Lu, D. Liu, Modified laser scanning technique in wavelength modulation spectroscopy for advanced TDLAS gas sensing, Opt. Laser Eng. (2022), 106906, https://doi.org/10.1016/j.optlaseng.2021.106906.

[12] A. Miklós, P. Hess, Z. Bozóki, Application of acoustic resonators in photoacoustic trace gas analysis, metrology, Rev. Sci. Instrum. 4 (2001) 1937–1955, https://doi.org/10.1063/1.1353198.

[13] H. Wu, L. Dong, X. Yin, A. Sampaolo, P. Patimisco, W. Ma, L. Zhang, W. Yin, L. Xiao, V. Spagnolo, S. Jia, Atmospheric CH4 measurement near a landfill using an ICL-based QEPAS sensor with V-T relaxation self-calibration, Sens. Actuators B Chem. (2019), 126753, https://doi.org/10.1016/j.snb.2019.126753.

[14] K. Chen, B. Zhang, S. Liu, Q. Yu, Parts-per-billion-level detection of hydrogen sulfide based on near-infrared all-optical photoacoustic spectroscopy, Sens. Actuators B Chem. 283 (2019) 1–5, https://doi.org/10.1016/j.snb.2018.11.163.

[15] W. Chen, B. Liu, H. Zhou, Y. Wang, C. Wang, Diode laser-based photoacoustic spectroscopy detection of acetylene gas and its quantitative analysis, Eur. Trans. Electr. Power 2 (2012) 226–234, https://doi.org/10.1002/etep.588.

[16] K. Chen, Q. Yu, Z. Gong, M. Guo, C. Qu, Ultra-high sensitive fiber-optic Fabry-Perot cantilever enhanced resonant photoacoustic spectroscopy, Sens. Actuators B Chem. (2018) 205–209, https://doi.org/10.1016/j.snb.2018.04.123.

[17] P. Fan, W. Yan, P. Lu, W. Zhang, W. Zhang, X. Fu, J. Zhang, High sensitivity fiber-optic Michelson interferometric low-frequency acoustic sensor based on a gold diaphragm, Opt. Express 17 (2020) 25238–25249, https://doi.org/10.1364/OE.402099.

[18] W. Zhang, P. Lu, W. Ni, W. Xiong, D. Liu, J. Zhang, Gold-diaphragm based fabry-perot ultrasonic sensor for partial discharge detection and localization, IEEE Photonics J. 3 (2020) 1–12, https://doi.org/10.1109/JPHOT.2020.2982460.

[19] Z. Gong, Y. Chen, T. Gao, K. Chen, Y. Jiao, M. Guo, B. Zhang, S. Liu, L. Mei, W. Peng, Q. Yu, Parylene-C diaphragm-based low-frequency photoacoustic sensor for space-limited trace gas detection, Opt. Laser Eng. (2020), 106288, https://doi.org/10.1016/j.optlaseng.2020.106288.

[20] Y. Tan, C. Zhang, W. Jin, F. Yang, H. Lut Ho, J. Ma, Optical fiber photoacoustic gas sensor with graphene nano-mechanical resonator as the acoustic detector, IEEE J. Sel. Top. Quant. 2 (2017) 199–209, https://doi.org/10.1109/JSTQE.2016.2606339.

[21] Y. Cao, R. Wang, J. Peng, K. Liu, W. Chen, G. Wang, X. Gao, Humidity enhanced N2O photoacoustic sensor with a 4.53 μm quantum cascade laser and Kalman filter, Photoacoustics (2021), 100303, https://doi.org/10.1016/j.pacs.2021.100303.

[22] Z. Gong, T. Gao, L. Mei, K. Chen, Y. Chen, B. Zhang, W. Peng, Q. Yu, Ppb-level detection of methane based on an optimized T-type photoacoustic cell and a NIR diode laser, Photoacoustics (2021), 100216, https://doi.org/10.1016/j.pacs.2020.100216.

[23] H. Jane, R.P. Tatam, Optical gas sensing: a review, Meas. Sci. Technol. 24 (1) (2012), 012004, https://doi.org/10.1088/0957-0233/24/1/012004.

[24] M. Sheplak, J. Dugundji, Large deflections of clamped circular plates under initial tension and transitions to membrane behavior, J. Appl. Mech. 65 (1998) 107–115, https://doi.org/10.1115/1.2789012.

[25] L.E. Kinsler, A.R. Frey, A.B. Coppens, J.V. Sanders. Fundamentals of Acoustics, fourth ed., John Wiley & Sons Inc, New York, 2001.

[26] L.B. Freund, S. Subra. Thin Film Materials: Stress, Defect Formation and Surface Evolution, first ed., Cambridge University Press, Cambridge, 2004, pp. 239–252.

[27] W. Zhang, P. Lu, Z. Qu, P. Fan, C. Sima, D. Liu, J. Zhang, High sensitivity and high stability dual fabry-perot interferometric fiber-optic acoustic sensor based on sandwich-structure composite diaphragm, IEEE Photonics J. 13 (2) (2021) 1–13, https://doi.org/10.1109/JPHOT.2021.3057666.

[28] Q. Yu, X. Zhou, Pressure sensor based on the fiber-optic extrinsic Fabry-Perot interferometer, Photon. Sens. 1 (2011) 72–83, https://doi.org/10.1007/s13320-010-0017-9.

[29] Z. Gong, K. Chen, Y. Chen, L. Mei, Q. Yu, Integration of T-type half-open photoacoustic cell and fiber-optic acoustic sensor for trace gas detection, Opt. Express 13 (2019) 18222, https://doi.org/10.1364/OE.27.018222.

[30] X. Yin, M. Gao, R. Miao, L. Zhang, X. Zhang, L. Liu, X. Shao, F.K. Tittel, Near-infrared laser photoacoustic gas sensor for simultaneous detection of CO and H2S, Opt. Express 21 (2021) 34258, https://doi.org/10.1364/OE.441698.

[31] L.S. Rothman, I.E. Gordon, Y. Babikov, A. Barbe, D. Chris Benner, P.F. Bernath, M. Birk, L. Bizzocchi, V. Boudon, L.R. Brown, A. Campargue, K. Chance, E. A. Cohen, L.H. Coudert, V.M. Devi, B.J. Drouin, A. Fayt, J.M. Flaud, R.R. Gamache, J.J. Harrison, J.M. Hartmann, C. Hill, J.T. Hodges, D. Jacquemart, A. Jolly, J. Lamouroux, R.J. Le Roy, G. Li, D.A. Long, O.M. Lyulin, C.J. Mackie, S.T. Massie, S. Mikhailenko, H.S.P. Müller, O.V. Naumenko, A.V. Nikitin, J. Orphal, V. Perevalov, A. Perrin, E.R. Polovtseva, C. Richard, M.A.H. Smith, E. Starikova, K. Sung, S. Tashkun, J. Tennyson, G.C. Toon, V.G. Tyuterev, G. Wagner, The HITRAN2012 molecular spectroscopic database, J. Quant. Spectrosc. Radiat. Transf. (2013) 4–50, https://doi.org/10.1016/j.jqsrt.2013.07.002.

[32] Y.P. Werle, R. Mücke, F. Slemr, The limits of signal averaging in atmospheric trace-gas monitoring by tunable diode-laser absorption spectroscopy (TDLAS), Appl. Phys. B Photo Laser Chem. 2 (1993) 131–139, https://doi.org/10.1007/BF00425997.

[33] M. Giglio, P. Patimisco, A. Sampaolo, G. Scamarcio, F.K. Tittel, V. Spagnolo, Allan deviation plot as a tool for Quartz-enhanced photoacoustic sensors noise analysis, IEEE Trans. Ultrason. Ferroelectr. Freq. Control 4 (2016) 555–560, https://doi.org/10.1109/TUFFC.2015.2495013.

[34] H. Zheng, M. Lou, L. Dong, H. Wu, W. Ye, X. Yin, C.S. Kim, M. Kim, W.W. Bewley, C.D. Merritt, C.L. Canedy, M.V. Warren, I. Vurgaftman, J.R. Meyer, F.K. Tittel, Compact photoacoustic module for methane detection incorporating interband cascade light emitting device, Opt. Express 14 (2017) 16761, https://doi.org/10.1364/OE.25.016761.

[35] R. Cui, L. Dong, H. Wu, W. Ma, L. Xiao, S. Jia, W. Chen, F.K. Tittel, Three-dimensional printed miniature fiber-coupled multipass cells with dense spot

patterns for PPB-level methane detection using a near-IR Diode Laser, Anal. Chem. 19 (2020) 13034–13041, https://doi.org/10.1021/acs.analchem.0c01931.
[36] Y. Li, R. Wang, F.K. Tittel, Y. Ma, Sensitive methane detection based on quartz-enhanced photoacoustic spectroscopy with a high-power diode laser and wavelet filtering, Opt. Laser Eng. (2020), 106155, https://doi.org/10.1016/j.optlaseng.2020.106155.
[37] C. Li, M. Guo, B. Zhang, C. Li, B. Yang, K. Chen, Miniature single-fiber photoacoustic sensor for methane gas leakage detection, Opt. Laser Eng. (2022), 106792, https://doi.org/10.1016/j.optlaseng.2021.106792.
[38] C. Lin, X. Yan, Y. Huang, An all-optical off-beam quartz-enhanced photoacoustic spectroscopy employing double-pass acoustic micro resonators, Opt. Commun. 503 (2022), 127447, https://doi.org/10.1016/j.optcom.2021.127447.

Hanping Xiao is now pursuing a master degree in optical engineering in School of Optical and Electronic Information at Huazhong University of Science and Technology, China. His research interests include optical sensors and photoacoustic spectroscopy.

Jinbiao Zhao is now pursuing a master degree in optical engineering in School of Optical and Electronic Information at Huazhong University of Science and Technology, China. His research interests include optical sensors and laser spectroscopy techniques.

Chaotan Sima is an Associate Professor at Huazhong University of Science and Technology, China. He obtained the Ph.D. degree at the Optoelectronics Research Centre in the University of Southampton UK in 2013. He has been awarded the Marie-Curie Fellowship in 2019 and IEEE senior member since 2021. His research interests include advanced optical gas sensing, planar waveguide devices and holey optical fiber. He has been granted over 10 projects from National Natural Science Foundation of China and the National Key Research and Development Program of China etc. He serves as an editorial member of Optical and Quantum Electronics.

Ping Lu is a Professor in School of Optical and Electronic Information at Huazhong University of Science and Technology, China, and Next Generation Internet Access National Engineering Laboratory. She got her Ph. D. degree on optical engineering in 2005 from Huazhong University of Science and Technology. Since 2006, she works at the School of Optical and Electronic Information at Huazhong University of Science and Technology, and starting from 2011, as full Professor. Her research mainly focused on fiber sensors, multicomponent trace gas detection, high sensitivity optical fiber acoustic detection technology, high resolution fiber sensor demodulation technology.

Yanhong Long is now pursuing a master degree in software engineering in School of Optical and Electronic Information at Huazhong University of Science and Technology, China, China. His research interests include gas sensors and photoacoustic spectroscopy.

Yan Ai is now pursuing a master degree in electronic information in School of Optical and Electronic Information at Huazhong University of Science and Technology, China. Her research interests include optical gas sensors and photoacoustic spectroscopy.

Wanjin Zhang is now pursuing a Ph.D. degree in optical engineering in School of Optical and Electronic Information at Huazhong University of Science and Technology, China. His research interests include optical sensors and laser spectroscopy techniques and high resolution fiber sensor demodulation technology.

Yufeng Pan received his master's degree in atomic and molecular physics from Shanxi University, China, in 2021. Currently he is a Ph.D. student in optical engineering at Huazhong University of Science and Technology. His research interests include optical sensors and laser spectroscopy techniques.

Jiangshan Zhang is an Associate Professor in School of Electronic Information and Communications at Huazhong University of Science and Technology, China. He obtained the Ph. D. degree on information and communication Engineering in 2005 from Huazhong University of Science and Technology. His research interests include signal processing and digital communication.

Deming Liu was born in Hubei Province, China, in January 1957. He received the Graduate degree from Chengdu Institute of Telecommunication (now University of Electronic Science and Technology of China), Chengdu, China, in 1984. Currently, he is the Professor of Huazhong University of Science and Technology, Wuhan, China. His recent research interests include optical access network, optical communication devices, and fiber-optic sensors.